PCCP

Configuration Mixing Upon Reorganization of Dihedral Angle Induces Rapid Intersystem Crossing in Organic Photoredox catalyst

Journal:	*Physical Chemistry Chemical Physics*
Manuscript ID	CP-ART-04-2020-001911.R1
Article Type:	Paper
Date Submitted by the Author:	25-May-2020
Complete List of Authors:	Kim, Hwon; Princeton University, Chemistry Scholes, Gregory; Princeton University, Chemistry

Configuration Mixing Upon Reorganization of Dihedral Angle Induces Rapid Intersystem Crossing in Organic Photoredox catalyst

*Hwon Kim and Gregory D. Scholes**

Department of Chemistry, Princeton University, Princeton, New Jersey 08544, United States

The authors declare no competing financial interest.

Corresponding Author

*E-mail: gscholes@princeton.edu

ABSTRACT: A long excited state lifetime is a desirable quality of photocatalysts because it enables a higher probability of energy or electron transfer from the photocatalyst to a substrate. However, achieving a long lifetime in organic (metal-free) catalysts is challenged by competing rapid nonradiative relaxation from excited states and relatively slow intersystem crossing into long-lived states with different spin multiplicity. In this work, we propose an intersystem crossing mechanism in heavy-metal free photocatalyst that results from reorganization of a dihedral angle between moieties. The relaxation of orthogonality of the dihedral angle and increasing the orbital

overlap between the two components of the molecule changes the coupling between the configurations of singlet and triplet states, which in turn results in larger spin orbit coupling between the two manifolds as the molecule twists. We predict that this enables intersystem crossing to outcompete the singlet state lifetime.

Introduction

Intersystem Crossing (ISC), the transition between electronic states of differing spin manifolds[1,2], has been leveraged in photocatalysis[3–8], light emitting diodes (LED)[9–12], triplet sensitization[13,14], photovoltaics[15,16], and therapeutics[17]. An important dichotomy of molecules that are used in ISC is the presence or absence of heavy atoms such as transition metals and halogens, which enable strong spin orbit coupling (SOC) and therefore promote ISC.[18,19] Heavy-metal free organic molecules,[20–24] for which ISC cannot be enabled by the heavy atom effect, nonetheless are of interest for photocatalysis due to the broad scope of reactions that can be achieved[21].

The most commonly used strategy for obtaining a high yield of excited triplet states in organic molecules has been design often based on El-Sayed's rule.[25–27] ISC can be facilitated by attaching functional groups that include non-bonding electrons or incorporating heavy halogens so that the heavy atom effect enhances SOC coupling. An alternative strategy does not aim for large SOC coupling, but long lifetime of the photoexcited state so that the molecule has adequate time to undergo ISC. For example, the exceptionally long lifetime of a phenoxazine derived photoredox catalyst[5,6] has been achieved by ensuring very small overlap of upper SOMO (Singly Occupied

Molecular Orbital) and lower SOMO. Small overlap in such cases derives from orbitals being oriented orthogonal to each other.

Exploiting orthogonality between local orbitals is in fact a widely used strategy for reverse intersystem crossing (RISC). For example, lack of overlap between orbitals that comprise a charge-transfer state[28–30] diminish the exchange splitting between singlet and triplet states, i.e. result in a very small singlet-triplet gap (ΔE_{ST}), so that thermal activation suffices to carry out RISC. The interplay of mechanisms of ISC in such systems can be difficult to pinpoint owing to the weak SOC between states with similar electronic configurations[31,32,41–44,33–40]. A large portion of the suggested alternative mechanisms take locally excited (LE) states into consideration, because there can be strong SOC between CT and LE states stemming from the orbital rotation. The recent work of de Silva et al.[44] proposed a four-state model that takes the configuration interaction into account to consider electronic states with mixed CT and LE character. The work shows that interplay of exchange integrals and one electron integrals of the orbitals can lead to different mixing strengths of configurations of the two spin multiplicities.

In this paper, we use quantum chemical calculations and the four-state model to study the ISC mechanism in the low-lying excited states of the photoredox catalyst, 3,7-(4-bi-phenyl)-1-naphthalene-10-phenoxazine (BPNP). BPNP has been extensively studied by Damrauer and co-workers[5–8] as a reducing photoredox catalyst with efficient ISC quantum yield, and serves as one of the few examples of exploiting the twisted structure to enhance singlet to triplet ISC. The molecule consists of a diphenyl phenoxazine and naphthalene moiety, as shown in Figure 1a.

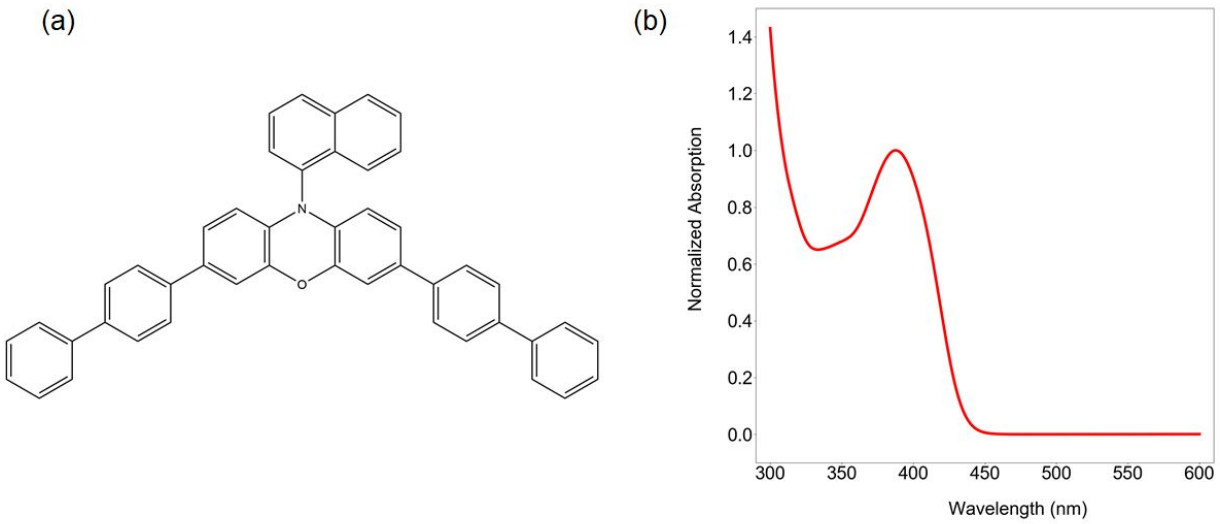

Figure 1. (a) The two-dimensional chemical structure of BPNP and (b) the steady state absorption spectrum of BPNP [Reference 6, presented with permission from Damrauer] (provided by the Damrauer group).

Photoexcitation of the BPNP to a bright state involves a transition between the phenoxazine ring and the diphenyl group, which is followed by internal conversion (IC) to a state which comprises charge transfer between the phenoxazine and naphthalene groups. The bright state will be denoted as $S_{CT\text{-}Biph}$ state, and the latter state will be denoted as $S_{CT\text{-}Naph}$ state from now on. The resulting $S_{CT\text{-}Naph}$ state is long-lived (45 ns lifetime), which leads to a remarkable ISC quantum yield of 0.9 to form the$T_{CT\text{-}Biph}$ state.[5,6].

Despite the compelling experimental results, the ISC mechanism has not been completely elucidated.[6] The question is whether the ISC involves a direct interaction between the $S_{CT\text{-}Naph}$ and the $T_{CT\text{-}Biph}$ state, which would be assisted by rotation of π-orbitals to induce strong SOC[5,6], or is it mediated by the $T_{CT\text{-}Naph}$ state, which is not expected to have strong SOC but can be coupled via hyperfine coupling?

To study more deeply the ISC pathway in BPNP, we employed quantum chemical calculations and the four-state model[44]. The electronic states and other relevant quantities for our analysis were calculated using the Complete Active Space Self-Consistent Field (CASSCF)[45] method to treat the electron correlation in a related rigorous manner. Even though there are no previous reports explicitly proposing a benchmark for related ISC rate calculations, CASSCF was chosen as it provides a rigorous wavefunction calculation by fully correlating the electrons in the active space, and has previously shown success in the study of an ISC pathway[46]. The electron correlation was shown to be crucial for obtaining correct singlet triplet gaps by de Silva, and thus is likely to be the reason TDDFT becomes inadequate.[47] A four-state model was exploited in order to obtain a succinct physical insight into state mixing, which is difficult in CASSCF owing to the large number of configurations included in the basis. The time dependent formalism based onFermi's Golden Rule, formulated by Etinski et al.[48–51] was employed to estimate k_{ISC}.

The results of our calculation suggest ISC to a triplet state with locally excited (LE) character on the naphthalene ring, which will be denoted as LE-Naph from now on, mixed with CT-Naph character as the intermediate state. The reorganization of the dihedral angle of phenoxazine and naphthalene molecular planes was found to play a cardinal role in modifying the configurations of the triplet states, bringing significant $T_{LE\text{-}Naph}$ character to what was originally exclusively $T_{CT\text{-}Naph}$. The result not only suggests the likely pathway of ISC in BPNP, but also can act as a guideline for increasing ISC efficiency from the systematic dependence of electronic state configuration on conformation.

Computational Methods

The geometry of BPNP was optimized for S_0, $S_{CT\text{-}Biph}$ and $S_{CT\text{-}Naph}$, $T_{CT\text{-}Biph}$, and $T_{LE\text{-}Naph}$ states. The geometry was optimized using Density Functional Theory (DFT) at the B3LYP/6-31G(d) level of theory for the S_0 state and Time Dependent DFT (TDDFT)[52] at the CAM-B3LYP/6-31G(d)[53] level of theory for all singlet excited states. The geometry of triplet states were optimized using TDDFT employing the Tamm-Dancoff Approximation (TDA),[54] noting the reported accuracy of TDA compared to conventional TDDFT for triplet states[55]. The polarizable continuum model was used to simulate the *N.N*-dimethylacetamide solvent, which was used in the experiments reported by the Damrauer group.[6] The optimized geometry for the ground state and the $S_{CT\text{-}Naph}$ state are shown in *Supplementary Information* to highlight the change of dihedral angle upon reorganization. Gaussian 16[56] was used in the geometry optimization step.

The optimized geometries were then used as input for single-point calculation with State Averaged Complete Active Space Self Consistent Field (SA-CASSCF)[45] followed by Strongly Contracted N-Electron Valence Perturbation Theory (SC-NEVPT2)[57], from which the wavefunctions and energies of states were obtained. For all geometries, with the exception of the ground state geometry, the two highest occupied molecular orbitals and the two lowest unoccupied orbitals from Restricted Hartree-Fock (RHF) calculation were included in the active space, which comprised 4 electrons and 4 orbitals. This was followed by SA-CASSCF averaging the five lowest triplet states and three lowest singlet states, from which the four optimized frontier orbitals were subsequently used in a further SA-CASSCF calculation with the five lowest triplet states and five lowest singlet states, averaging over 10 states in total. In the case of the singlet ground state geometry, using natural orbitals from the preliminary SA-CASSCF calculation failed

to converge, and thus RHF orbitals were directly used. The single point calculations were performed with Ahlrich's def2-SVP basis with coulomb and exchange fitting[58,59], with the N,N-dimethylacetamide solvent added through SMD solvation model.[60] All of the single-point energy calculations were performed with ORCA software[61,62].

To quantify the contribution of the $T_{LE\text{-}Naph}$ state to the ISC process, the cumulant expansion of Etinski et al.[48] was used, which calculates k_{ISC} under the Condon approximation by using the Heisenberg picture of Fermi's Golden Rule. The details of the formula will be explained in the *Supplementary Information.* The form of the rate equation is

$$\boldsymbol{k_{ISC} = 2\left|\langle T \left| \hat{H}_{SOC} \right| S\rangle\right|^2 e^{-\kappa_2^{R,TI}} \int_0^\infty \cos\left(\kappa_1 t + \kappa_2^{Im}\right) e^{-\kappa_2^{R,TD}} dt} \quad (1)$$

which contains the SOC matrix element, Duschinsky matrix, displacement vector, and adiabatic energy gap of singlet and triplet states. The Duschinsky matrix and displacement vector were calculated using Gaussian 16[56] software, and the SOC matrix element was obtained between SA-CASSCF states using ORCA software[61,62].

Results and Discussion

SA-CASSCF Calculation

The optimized orbitals from the SA-CASSCF calculations are depicted in Figure 2a, 2b, 2c, and 2d, showing two orbitals with higher density of electrons on the phenoxazine moiety compared to the naphthalene moiety, and two orbitals with higher density of electrons on the naphthalene moiety compared to the phenoxazine moiety. Figure 2e shows the MO diagrams of the configurations that play a role in the ISC process.

Table 1 collects the vertical energies, adiabatic energies and transition dipoles from SA-CASSCF-NEVPT2 and the optimized dihedral angle of singlet states, confirming that the $S_{CT\text{-}Naph}$ is the lower singlet state of the molecule. The dihedral angle was measured using the scheme shown in Figures 3a and 3b. The bright state, $S_{CT\text{-}Biph,}$ is predicted to have a transition energy of 3.19 eV, matching the experimental transition energy of 3.20 eV very well.

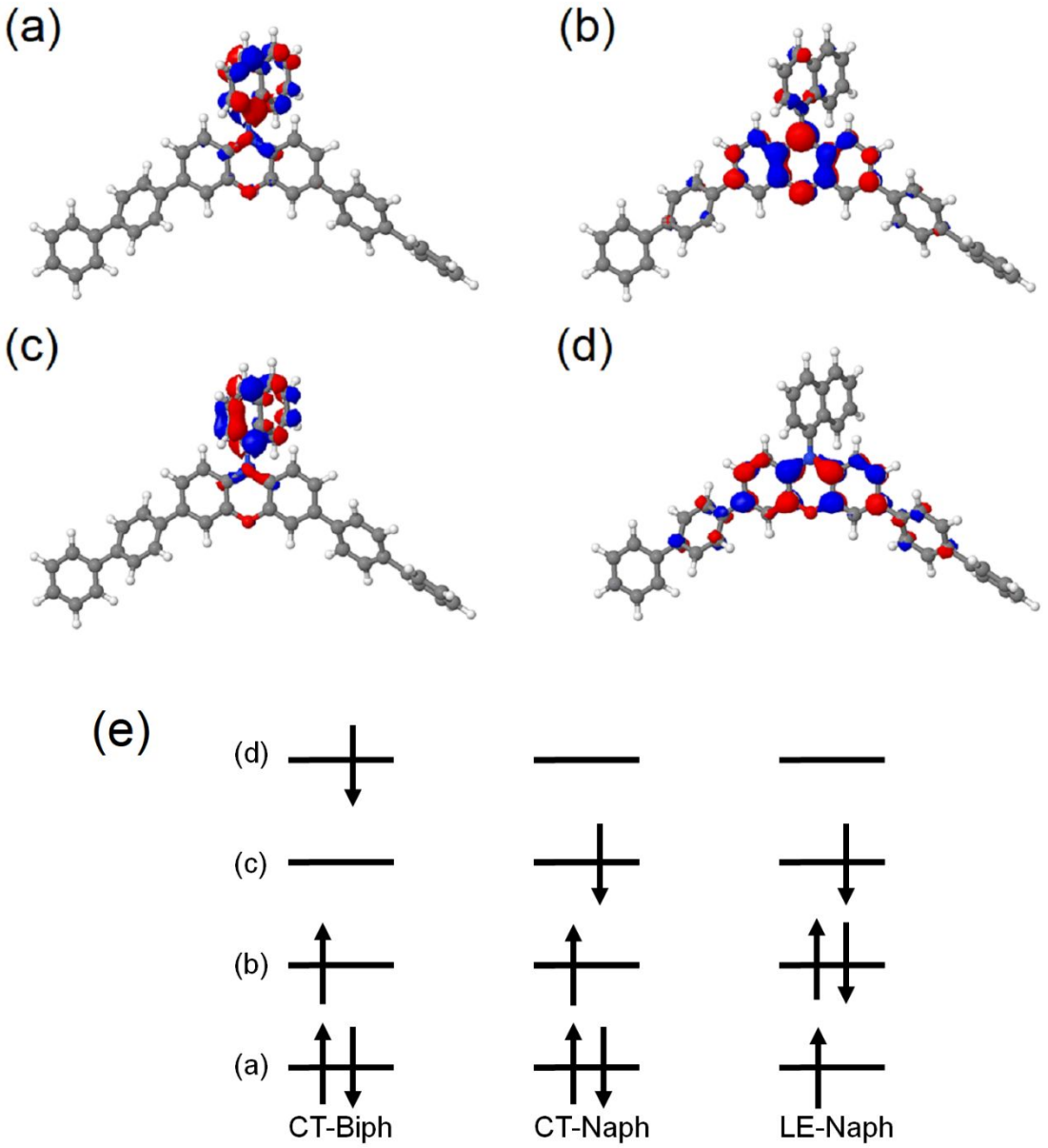

Figure 2. (a), (b), (c), and (d) are the four natural orbitals of BPNP from SA-CASSCF at $S_{CT\text{-}Naph}$ optimized geometry, in order of decreasing occupancy at the ground state. As shown in the isosurface plot, orbitals (a) and (c) have higher electron density on the naphthalene moiety, while orbitals (b) and (d) have higher electron density on the phenoxazine moiety. (e) shows the MO

diagram of configurations considered in this work, where the CT-Naph and LE-Naph states are included in the four-state model.

Table 1. The transition energy, adiabatic energy (0-0 energy), and transition dipole of the two lowest singlet states and the dihedral angle at the respective optimized geometry.

State	Vertical Energy (eV)	Adiabatic Energy (eV)	Transition Dipole (Debye)	Dihedral Angle
$S_{CT\text{-}Naph}$	3.18	2.88	0.44	70.8
$S_{CT\text{-}Biph}$	3.19	2.91	6.49	89.6

The SA-CASSCF calculation shows that the triplet CT-Naph and triplet LE-Naph configurations are drastically mixed by decreasing the dihedral angle, while the singlet counterparts mix only to a small degree. Despite the mixed configuration, the triplet states will still be denoted as $T_{CT\text{-}Naph}$ and $T_{LE\text{-}Naph}$ according to the parent configuration for convenience.

The degree of mixing of configurations was quantified by the difference of the square of the coefficients of the CT-Naph configuration and LE-Naph configuration, denoted as ΔP. This quantity is plotted with respect to the dihedral angle in Figure 3d. The effect of configuration interaction on the energy of triplet states is manifested in the energy levels of the states, which are shown in Figure 3c. At a dihedral angle of 90 degrees, $S_{CT\text{-}Naph}$ and $T_{CT\text{-}Naph}$ are very close in energy as is expected from the vanishing orbital overlap. $T_{LE\text{-}Naph}$ is higher in energy than $S_{CT\text{-}Naph}$, making ISC to $T_{LE\text{-}Naph}$ unfavorable at this particular geometry. On the other hand, at the optimized

geometry of $S_{CT\text{-}Naph}$, with the dihedral angle of 70.8 degrees, the $T_{LE\text{-}Naph}$ state falls slightly below the $S_{CT\text{-}Naph}$ state, making the state a promising final state in the ISC pathway.

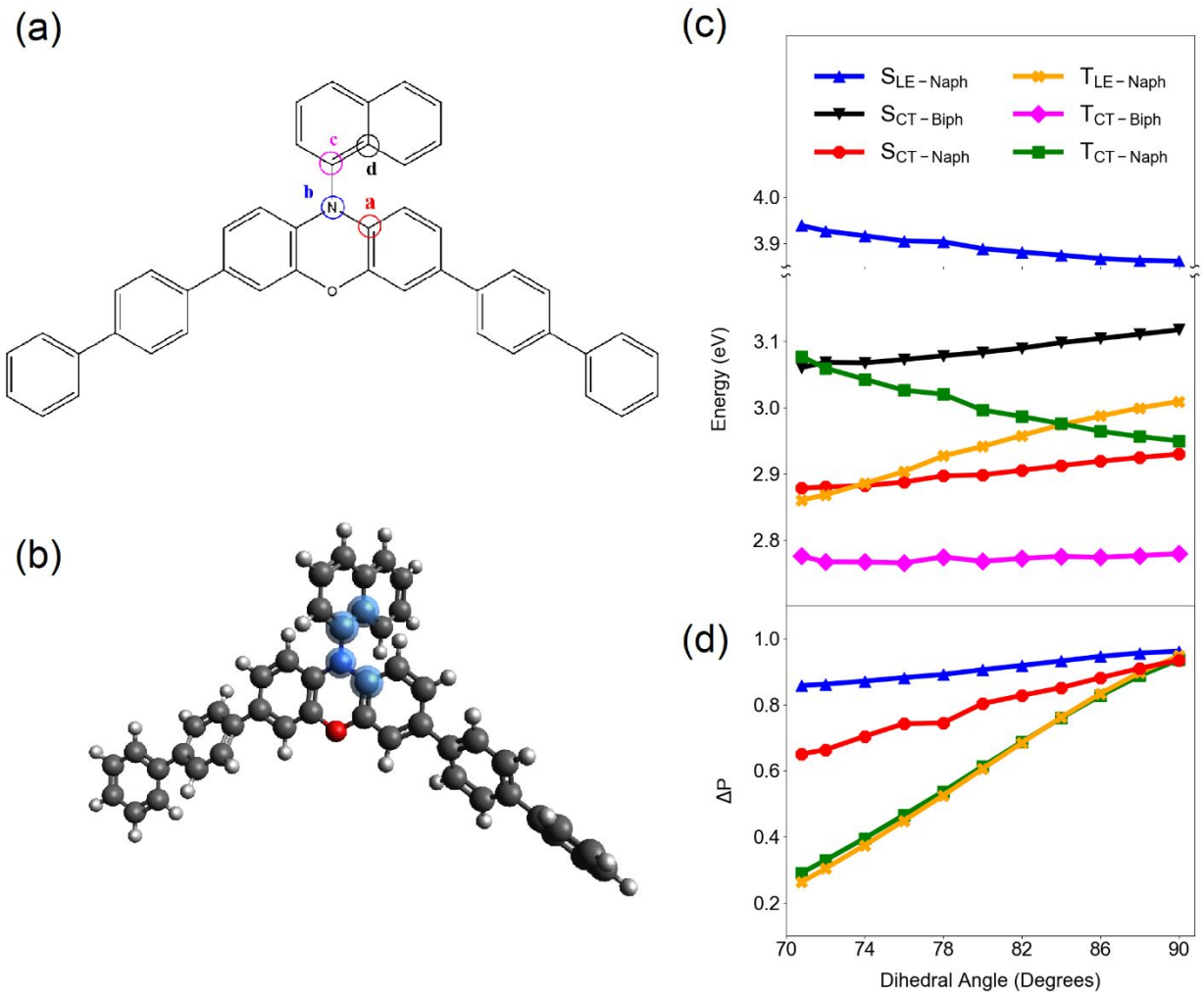

Figure 3. (a) and (b) show the atoms used in defining of the dihedral angle used in this paper in 2D and 3D structure of BPNP, respectively. One plane is defined by the plane a-b-c and one is defined by the plane b-c-d in (a). (c) shows the SA-CASSCF-NEVPT2 energy dependence on dihedral angle, with the energy of ground state at its relaxed geometry set as the reference point. (d) shows ΔP obtained from SA-CASSCF wavefunctionfor LE-Naph and CT-Naph states of singlet

and triplet manifold are plotted as a function of dihedral angle. The ΔP is defined as $\left||c_{CT-Naph}|^2 - |c_{LE-Naph}|^2\right|$, which is 0 for completely mixed state and 1 for single configuration state. The legend is based on that of plot (c), where the states are labelled according to the configuration with the largest absolute value of coefficient.

Four State Model

The difference in degree of mixing predicted by the SA-CASSCF calculations can be understood through the four-state model[44,47], which simplifies the basis into four states. The singlet and triplet states of CT-Naph and LE-Naph states were taken into consideration because the configuration interaction of the two configurations was the most drastic. The Hamiltonian matrix in the basis of configuration state function (CSF) of the $S_{CT\text{-}Naph}$, $S_{LE\text{-}Naph}$, $T_{CT\text{-}Naph}$, and $T_{LE\text{-}Naph}$ without mixing between different configurations is:

$$\boldsymbol{H_S} = \begin{bmatrix} \boldsymbol{K_{CT}} & \boldsymbol{t - K_X} \\ \boldsymbol{t - K_X} & \boldsymbol{\Delta E + K_{LE}} \end{bmatrix}, \boldsymbol{H_T} = \begin{bmatrix} \boldsymbol{-K_{CT}} & \boldsymbol{t + K_X} \\ \boldsymbol{t + K_X} & \boldsymbol{\Delta E - K_{LE}} \end{bmatrix} \quad (2)$$

which is block diagonalized into a singlet Hamiltonian and a triplet partition. Denoting the occupied and unoccupied orbitals localized on the naphthalene ring as ϕ_a and ϕ_c, respectively, the occupied and unoccupied orbitals localized on phenoxazine ring as ϕ_b and ϕ_d, respectively, and the core orbitals as *i*, and denoting the Coulomb integral as

$$\langle \boldsymbol{ab} \,|\, \boldsymbol{cd} \rangle = \int_{-\infty}^{+\infty} \boldsymbol{dr_1} \int_{-\infty}^{+\infty} \boldsymbol{dr_2} \boldsymbol{\phi_a^*}(\boldsymbol{r_1}) \boldsymbol{\phi_b^*}(\boldsymbol{r_2}) \frac{\mathbf{1}}{|\boldsymbol{r_1 - r_2}|} \boldsymbol{\phi_c}(\boldsymbol{r_1}) \boldsymbol{\phi_d}(\boldsymbol{r_2}) \quad (3)$$

The parameters in Hamiltonian matrix can be expressed as:

$$\mathbf{t} = \langle \boldsymbol{a} \,|\, \boldsymbol{b} \rangle + \sum_{\boldsymbol{i}=\mathbf{1}}^{\boldsymbol{core}} (\langle \boldsymbol{ai} \,|\, \boldsymbol{bi} \rangle - \langle \boldsymbol{ai} \,|\, \boldsymbol{ib} \rangle) + \langle \boldsymbol{aa} \,|\, \boldsymbol{ba} \rangle + \langle \boldsymbol{ab} \,|\, \boldsymbol{bb} \rangle + \langle \boldsymbol{ac} \,|\, \boldsymbol{bc} \rangle - \langle \boldsymbol{ac} \,|\, \boldsymbol{cb} \rangle \quad (4)$$

$$\boldsymbol{K_{CT}} = \langle \boldsymbol{bc} \,|\, \boldsymbol{cb} \rangle \tag{5}$$

$$\boldsymbol{K_{LE}} = \langle \boldsymbol{ac} \,|\, \boldsymbol{ca} \rangle \tag{6}$$

$$\boldsymbol{K_{X}} = \langle \boldsymbol{ac} \,|\, \boldsymbol{cb} \rangle \tag{7}$$

Also, ΔE corresponds to the energy gap between CT-Naph and LE-Naph configurations without spin adaptation. Defining $J_S = t - K_X$, $J_T = t + K_X$, $\Delta E_S = \Delta E + K_{LE} - K_{CT}$ and $\Delta E_T = \Delta E + K_{CT} - K_{LE}$, diagonalization of the Hamiltonian yields ΔP as

$$\Delta \boldsymbol{P_{S/T}} = \frac{\mathbf{1}}{\sqrt{\mathbf{1} + \mathbf{4}\dfrac{|\boldsymbol{J_{S/T}}|^2}{\Delta \boldsymbol{E_{S/T}^2}}}} \tag{8}$$

The ΔP, $|J_{S/T}|$, $\Delta E_{S/T}$ were calculated from RHF orbitals and are plotted in Figure 4 to demonstrate their dependence on the dihedral angle. The four-state model qualitatively reproduces the more drastic decrease of ΔP in the triplet manifold as a function of decreasing dihedral angle, while providing three important physical insights. First, the K_{LE} integral brings the energy of $T_{LE\text{-}Naph}$ state below that of $T_{CT\text{-}Naph}$ state to reverse the energy ordering. Second, smaller absolute values of ΔE_T are seen at smaller dihedral angles, which is caught mainly by the cancelling of K_{LE} by increasing ΔE, which, in turn, stems from stabilization of the CT-Naph state. This near degeneracy of triplet CSF is the dominant reason for the low ΔP of the triplet manifold. Finally, the increased magnitude of the transfer integral (t) and the LE-CT exchange integral (K_X) upon increase of overlap between the orbitals on two phenoxazine and naphthalene moieties gives larger coupling

between the triplet states, which increases the energy splitting of $T_{CT\text{-}Naph}$ and $T_{LE\text{-}Naph}$. Figure S5 in *Supplementary Information* demonstrates that dynamic correlation effect from NEVPT2 must be taken into account to observe crossing of the $T_{CT\text{-}Naph}$ with the $T_{LE\text{-}Naph}$ energy.

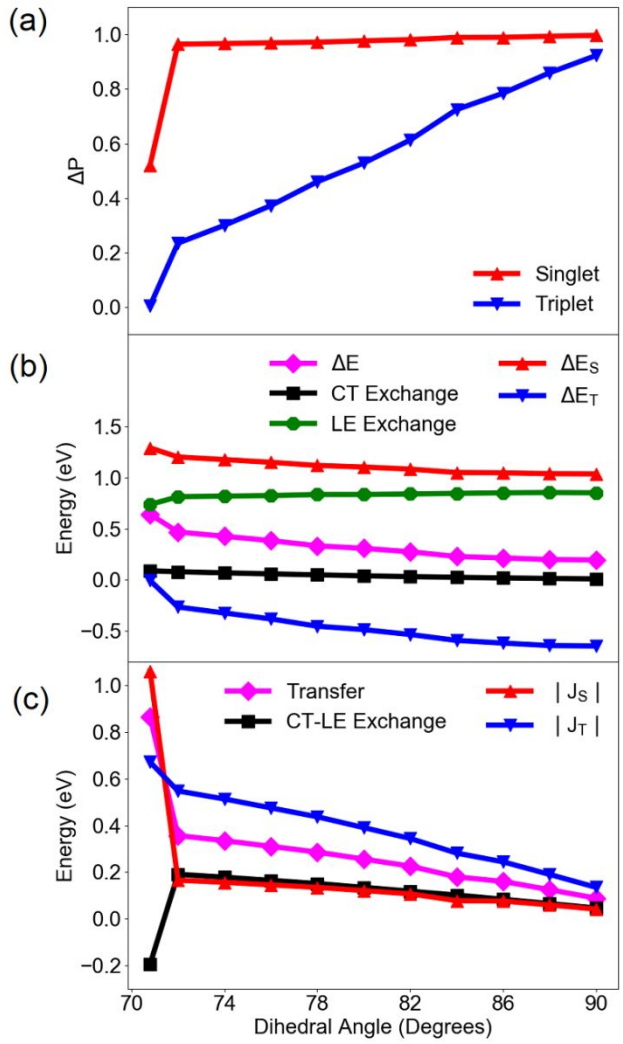

Figure 4. (a) ΔP calculated from the four-state model, reproducing the result from CASSCF calculation in Figure 3d. (b) The value of four-state model parameters that contribute to ΔE_S and ΔE_T are shown along with the curves for ΔE_S and ΔE_T. (c) The value of four-state model parameters that contribute to J_S and J_T are shown along with the curves for J_S and J_T.

ISC Rate Calculation

The optimized structure of $S_{CT\text{-}Naph}$ was assumed to be the geometry most relevant to the ISC process, from which the manifold of electronic states, the spin orbit coupling matrix element between $S_{CT\text{-}Naph}$ and the low-lying triplet states were obtained. The adiabatic energy gap of the triplet states with respect to $S_{CT\text{-}Naph}$, (ΔE_{ST}) the SOC matrix element, and the calculated ISC time constant (τ_{ISC}) are listed in Table 2. The ISC scheme is depicted in Figure 5, together with the energy alignment at ground state geometry (which was the scheme considered previously) for comparison.

Table 2. The adiabatic energy gap of triplet states and $S_{CT\text{-}Naph}$ state, the SOC element, and the ISC time constant

State	ΔE_{ST} (eV)	Integral (a.u.)	SOC (cm^{-1})	τ_{ISC} (ns)
$T_{CT\text{-}Biph}$	0.12	0.24	0.85	3317.61
$T_{LE\text{-}Naph}$	0.15	150.47	1.46	1.44

Despite the rather weak SOC, the mixing of configurations is nevertheless crucial; the calculated SOC between $S_{CT\text{-}Naph}$ and $T_{CT\text{-}Naph}$ at the ground state geometry is 0.11 cm^{-1}, which would not enable rapid ISC and demonstrates the dependence of ISC rate to the geometry. The ISC rate to $T_{CT\text{-}Biph}$ is three orders of magnitude slower than ISC to $T_{LE\text{-}Naph,}$ which can be explained by the small adiabatic energy gap compared to the large distortion of geometry, which puts the curve crossing point far away from the $S_{CT\text{-}Naph}$ geometry, as can be seen from Figure 3c, where the $T_{LE\text{-}Naph}$ and $S_{CT\text{-}Naph}$ cross in the vicinity of the $S_{CT\text{-}Naph}$ geometry, while the $T_{CT\text{-}Biph}$ curve consistently lies below that of $S_{CT\text{-}Naph}$ and thus implies high barrier to the transition. This is

confirmed by varying the adiabatic energy gap between $S_{CT\text{-}Naph}$ and $T_{CT\text{-}Biph}$, in which the value of the integral increases as the adiabatic energy gap increases from the calculated value. The trend is shown in Figure S8 of *Supplementary Information.* It should also be noted that the ΔE_{ST} of $T_{LE\text{-}Naph}$ might be overestimated in this dataset from SA-CASSCF averaging over 5 singlets and 5 triplets, which was employed due to the well behaved convergence for all geometries and to encompass all the states of interest. ΔE_{ST} of $T_{LE\text{-}Naph}$ becomes smaller than $T_{CT\text{-}Biph}$ in other averaging schemes, which explains the final triplet state having CT-Biph character in experimental work.[6,7] Even though the quantitative accuracy of the calculations cannot be assured, the preferred ISC pathway can be asserted to involve $T_{LE\text{-}Naph}$ state, because the difference in rate of two pathways is very drastic and smaller ΔE_{ST} will lead to faster ISC. The ΔE_{ST} values calculated from other averaging schemes are shown in Table S1 of *Supplementary Information.*

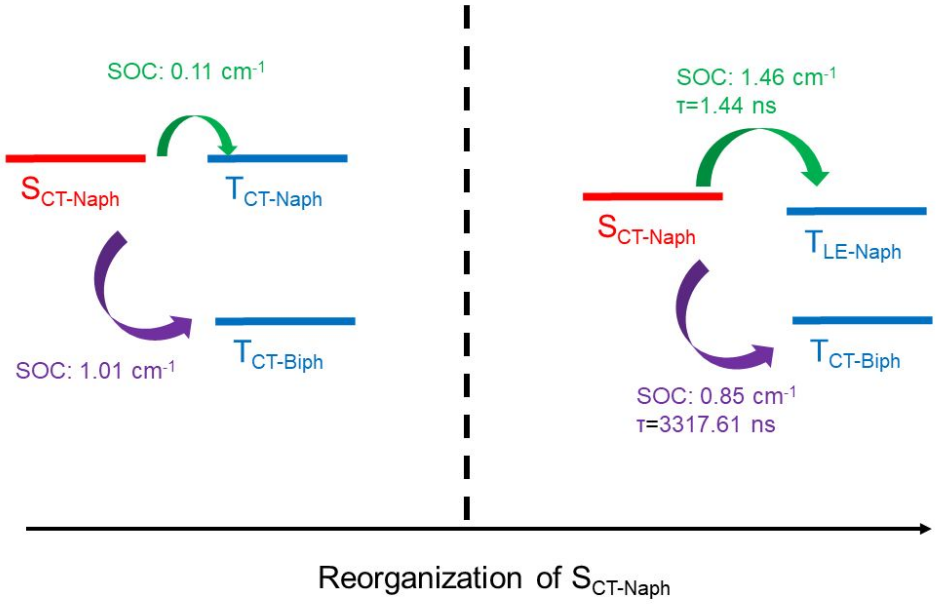

Figure 5. The scheme of ISC in BPNP is shown on the right side of the figure, which is compared with the energetic alignment at ground state geometry, shown on the left side of the figure. The

SOC to $T_{CT\text{-}Naph}$ state at S_0 geometry is very weak as speculated, which has brought ambiguity to the ISC mechanism. Only after the mixing of configurations, the SOC becomes strong enough to outcompete the relaxation back to ground state, which was measured to have time constant of 45 ns from experimental findings of Damrauer group.[6]

Conclusion

The ISC of BPNP is made possible by the mixing of triplet state configurations that results in enhanced SOC. From a quantum chemical perspective, this result serves as an example of mixing of configurations via variation of a particular nuclear degree of freedom. Therefore, our work highlights that diabatic states with one configuration may not be an adequate description of such electronic states. Furthermore, the four-state model decomposes the diagonal energy and coupling into integrals that change intuitively with orbital overlap, thereby giving a concise explanation of the configuration mixing predicted by ab-initio quantum chemistry methods. For the purpose of designing efficient ISC in organic photocatalysts, our results gives a guideline for exploiting molecules with orthogonal moieties. The analysis from the four-state model adds importance to the strategy of using either electron donating or withdrawing groups[7] because the near-degeneracy of LE and CT CSFs has been found to be crucial to having electronic states with mixed character. Furthermore, exploration of solvent effects on ISC efficiency will also be encouraged because the reorganization of charge transfer states may vary substantially depending on solvent polarity and viscosity.

Electronic Supplementary Information (ESI) Available:

Molecular structure and atomic coordinates of optimized geometry for S_0 state, $S_{CT\text{-}Naph}$ state, $T_{Naph\ Local}$ state, and $T_{CT\text{-}Biph}$ state, effect of dynamic correlation to the curve crossing of $T_{CT\text{-}Naph}$ and $T_{Naph\ Local}$ states, details of the ISC rate equation used, Duschinsky matrix, displacement vector, and the time-dependent cumulant expansion function from ISC rate calculation, calculations of integrals in the four-state model, ISC rate calculated from the adiabatic energy of CASSCF with different averaging scheme (PDF)

AUTHOR INFORMATION

Corresponding Author

Email: gscholes@princeton.edu

Conflicts of Interest

The authors declare no competing financial interests.

ACKNOWLEDGMENT

Financial support was provided by the Division of Chemical Sciences, Geosciences, and Biosciences, Office of Basic Energy Sciences of the U.S. DOE through Grant No. DE-SC0019370. Gregory Scholes is a CIFAR Fellow in the Bio-Inspired Energy Program.

REFERENCES

1 N. J. Turro, V. Ramamurthy and J. C. Scaiano, *Principles of molecular photochemistry: an introduction*, University science books, 2009.

2 M. Klessinger and J. Michl, *Excited States and Photochemistry of Organic Molecules*, Wiley-VCH, 1995.

3 W. Li, L. Li, H. Xiao, R. Qi, Y. Huang, Z. Xie, X. Jing and H. Zhang, *RSC Adv.*, 2013, **3**, 13417–

13421.

4 K. Rangan, S. M. Arachchige, J. R. Brown and K. J. Brewer, *Energy Environ. Sci.*, 2009, **2**, 410–419.

5 Y. Du, R. M. Pearson, C. H. Lim, S. M. Sartor, M. D. Ryan, H. Yang, N. H. Damrauer and G. M. Miyake, *Chem. - A Eur. J.*, 2017, **23**, 10962–10968.

6 S. M. Sartor, B. G. McCarthy, R. M. Pearson, G. M. Miyake and N. H. Damrauer, *J. Am. Chem. Soc.*, 2018, **140**, 4778–4781.

7 S. M. Sartor, C. H. Chrisman, R. M. Pearson, G. M. Miyake and N. H. Damrauer, *J. Phys. Chem. A*, 2020, **124**, 817–823.

8 S. M. Sartor, Y. M. Lattke, B. G. McCarthy, G. M. Miyake and N. H. Damrauer, *J. Phys. Chem. A*, 2019, **123**, 4727–4736.

9 C. Adachi, M. A. Baldo, M. E. Thompson and S. R. Forrest, *J. Appl. Phys.*, 2001, **90**, 5048–5051.

10 H. Uoyama, K. Goushi, K. Shizu, H. Nomura and C. Adachi, *Nature*, 2012, **492**, 234–238.

11 K. Goushi, K. Yoshida, K. Sato and C. Adachi, *Nat. Photonics*, 2012, **6**, 253–258.

12 Q. Peng, D. Fan, R. Duan, Y. Yi, Y. Niu, D. Wang and Z. Shuai, *J. Phys. Chem. C*, 2017, **121**, 13448–13456.

13 H. C. Chen, C. Y. Hung, K. H. Wang, H. L. Chen, W. S. Fann, F. C. Chien, P. Chen, T. J. Chow, C. P. Hsu and S. S. Sun, *Chem. Commun.*, 2009, 4064–4066.

14 Z. D. Miller, B. J. Lee and T. P. Yoon, *Angew. Chemie - Int. Ed.*, 2017, **56**, 11891–11895.

15 C. M. Yang, C. H. Wu, H. H. Liao, K. Y. Lai, H. P. Cheng, S. F. Horng, H. F. Meng and J. T. Shy, *Appl. Phys. Lett.*, 2007, **90**, 1–4.

16 Z. Xu, B. Hu and J. Howe, *J. Appl. Phys.*, , DOI:10.1063/1.2885349.

17 J. Tatchen, N. Gilka and C. M. Marian, *Phys. Chem. Chem. Phys.*, 2007, **9**, 5209–5221.

18 S. P. McGlynn, J. Daigre and F. J. Smith, *J. Chem. Phys.*, 1963, **39**, 675–679.

19 A.Juris, V.Balzani, F.Barigelletti, S.Campagna, P.Belser and A. vo. Zelewsky, *Coord. Chem. Rev.*, 1988, **84**, 85–277.

20 N. J. Treat, H. Sprafke, J. W. Kramer, P. G. Clark, B. E. Barton, J. Read De Alaniz, B. P. Fors and C. J. Hawker, *J. Am. Chem. Soc.*, 2014, **136**, 16096–16101.

21 N. A. Romero and D. A. Nicewicz, *Chem. Rev.*, 2016, **116**, 10075–10166.

22 H. D. Burrows, J. S. De Melo, C. Serpa, L. G. Arnaut, A. P. Monkman, I. Hamblett and S. Navaratnam, *J. Chem. Phys.*, 2001, **115**, 9601–9606.

23 S. Ji, J. Ge, D. Escudero, Z. Wang, J. Zhao and D. Jacquemin, *J. Org. Chem.*, 2015, **80**, 5958–5963.

24 W. Wu, X. Cui and J. Zhao, *Chem. Commun.*, 2013, **49**, 9009–9011.

25 Z. He, W. Zhao, J. W. Y. Lam, Q. Peng, H. Ma, G. Liang, Z. Shuai and B. Z. Tang, *Nat. Commun.*, 2017, **8**, 1–7.

26 M. A. El-Sayed, *Acc. Chem. Res.*, 1968, **1**, 8–16.

27 J. Zhao, K. Chen, Y. Hou, Y. Che, L. Liu and D. Jia, *Org. Biomol. Chem.*, 2018, **16**, 3692–3701.

28 W. Rettig, *J. Phys. Chem.*, 1982, **86**, 1970–1976.

29 W. Rettig and E. A. Chandross, *J. Am. Chem. Soc.*, 1985, **107**, 5617–5624.

30 W. Rettig, *Angew. Chemie Int. Ed. English*, 1986, **25**, 971–988.

31 J. Gibson, A. P. Monkman and T. J. Penfold, *ChemPhysChem*, 2016, 2956–2961.

32 M. K. Etherington, J. Gibson, H. F. Higginbotham, T. J. Penfold and A. P. Monkman, *Nat. Commun.*, 2016, **7**, 1–7.

33 B. T. Lim, S. Okajima, A. K. Chandra and E. C. Lim, *Chem. Phys. Lett.*, 1981, **79**, 22–27.

34 T. Ogiwara, Y. Wakikawa and T. Ikoma, *J. Phys. Chem. A*, 2015, **119**, 3415–3418.

35 T. J. Penfold, E. Gindensperger, C. Daniel and C. M. Marian, *Chem. Rev.*, 2018, **118**, 6975–7025.

36 X. K. Chen, S. F. Zhang, J. X. Fan and A. M. Ren, *J. Phys. Chem. C*, 2015, **119**, 9728–9733.

37 C. M. Marian, *J. Phys. Chem. C*, 2016, **120**, 3715–3721.

38 P. K. Samanta, D. Kim, V. Coropceanu and J. L. Brédas, *J. Am. Chem. Soc.*, 2017, **139**, 4042–4051.

39 K. Lee and D. Kim, *J. Phys. Chem. C*, 2016, **120**, 28330–28336.

40 F. B. Dias, J. Santos, D. R. Graves, P. Data, R. S. Nobuyasu, M. A. Fox, A. S. Batsanov, T. Palmeira, M. N. Berberan-Santos, M. R. Bryce and A. P. Monkman, *Adv. Sci.*, 2016, **3**, 1–10.

41 T. Hosokai, H. Noda, H. Nakanotani, T. Nawata, Y. Nakayama, H. Matsuzaki and C. Adachi, *J. Photonics Energy*, 2018, **8**, 1.

42 L. Gan, K. Gao, X. Cai, D. Chen and S. J. Su, *J. Phys. Chem. Lett.*, 2018, 9, 4725–4731.

43 R. S. Nobayasu, Z. Ren, G. C. Griffiths, A. S. Batsanov, P. Data, S. Yan, A. P. Monkman, M. R. Bryce and F. B. Dias, *Adv. Opt. Mater.*, 2016, **4**, 597–607.

44 P. De Silva, C. A. Kim, T. Zhu and T. Van Voorhis, *Chem. Mater.*, 2019, **31**, 6995–7006.

45 B. O. Roos, *Int. J. Quantum Chem.*, 1980, **18**, 175–189.

46 E. J. Taffet, D. Beljonne, Y. Olivier, F. Lam and G. D. Scholes, *J. Phys. Chem. Lett.*, 2018, **9**, 1620–1626.

47 P. De Silva, *J. Phys. Chem. Lett.*, 2019, **10**, 5674–5679.

48 M. Etinski, J. Tatchen and C. M. Marian, *J. Chem. Phys.*, 2011, **134**, 154105.

49 J. Föller, M. Kleinschmidt and C. M. Marian, *Inorg. Chem.*, 2016, **55**, 7508–7516.

50 L. Paul, T. Moitra, K. Ruud and S. Chakrabarti, *J. Phys. Chem. Lett.*, 2019, **10**, 369–374.

51 T. Moitra, M. M. Alam and S. Chakrabarti, *Phys. Chem. Chem. Phys.*, 2018, **20**, 23244–23251.

52 E. Runge and E. K. U. Gross, *Phys. Rev. Lett.*, 1984, **52**, 997.

53 T. Yanai, D. P. Tew and N. C. Handy, *Chem. Phys. Lett.*, 2004, **393**, 51–57.

54 S. Hirata and M. Head-Gordon, *Chem. Phys. Lett.*, 1999, **314**, 291–299.

55 M. J. G. Peach, M. J. Williamson and D. J. Tozer, *J. Chem. Theory Comput.*, 2011, **7**, 3578–3585.

56 M. J. Frisch, G. W. Trucks, H. B. Schlegel and D. J. F. G. E. Scuseria, M. A. Robb, J. R. Cheeseman, G. Scalmani, V. Barone, G. A. Petersson, H. Nakatsuji, X. Li, M. Caricato, A. V. Marenich, J. Bloino, B. G. Janesko, R. Gomperts, B. Mennucci, H. P. Hratchian, J. V., 2016.

57 C. Angeli, R. Cimiraglia, S. Evangelisti, T. Leininger and J. P. Malrieu, *J. Chem. Phys.*, 2001, **114**, 10252.

58 F. Weigend and R. Ahlrichs, *Phys. Chem. Chem. Phys.*, 2005, **7**, 3297–3305.

59 F. Weigend, *J. Comput. Chem.*, 2008, **29**, 167–175.

60 A. V. Marenich, C. J. Cramer and D. G. Truhlar, *J. Phys. Chem. B*, 2009, **113**, 6378–6396.

61 F. Neese, *Wiley Interdiscip. Rev. Comput. Mol. Sci.*, 2012, **2**, 73–78.

62 F. Neese, *Wiley Interdiscip. Rev. Comput. Mol. Sci.*, 2018, **8**, 4–9.

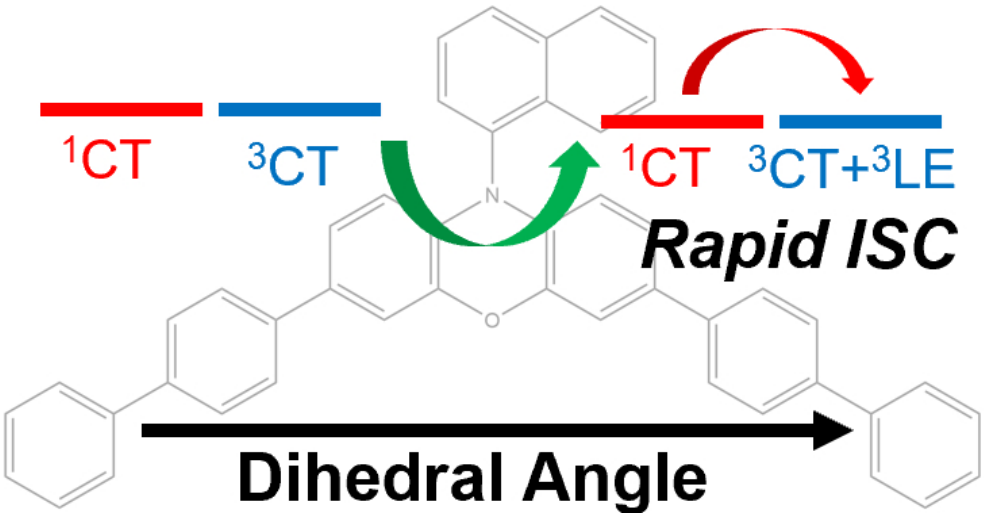

78x39mm (240 x 240 DPI)